

A pseudo-thermodynamic description of dispersion for nanocomposites



Yan Jin ^a, Gregory Beaucage ^{a,*}, Karsten Vogtt ^a, Hanqiu Jiang ^a, Vikram Kuppala ^b, Jay Kim ^c, Jan Ilavsky ^d, Mindaugas Rackaitis ^c, Andrew Mulderig ^a, Kabir Rishi ^a, Vishak Narayanan ^a

^a University of Cincinnati, Cincinnati OH 45242-0012, United States

^b University of Dayton, Dayton OH 45469, United States

^c Bridgestone Americas Center for Research and Technology, Akron OH 44301, United States

^d Advanced Photon Source, Argonne National Laboratory, Argonne IL 60439, United States

ARTICLE INFO

Article history:

Received 24 July 2017

Received in revised form

11 September 2017

Accepted 16 September 2017

Available online 18 September 2017

Keywords:

Nanocomposite

Reinforced elastomer

Small-angle scattering

Virial approach

Dispersion

Compatibility

Polybutadiene

Polyisoprene

Silica

Carbon black

ABSTRACT

Dispersion in polymer nanocomposites is determined by the kinetics of mixing and chemical affinity. Compounds like reinforcing filler/elastomer blends display some similarity to colloidal solutions in that the filler particles are close to randomly dispersed through processing. It is attractive to apply a pseudo-thermodynamic approach taking advantage of this analogy between the kinetics of mixing for polymer compounds and thermally driven dispersion for colloids. In order to demonstrate this pseudo-thermodynamic approach, two polybutadienes and one polyisoprene were milled with three carbon blacks and two silicas. These samples were examined using small-angle x-ray scattering as a function of filler concentration to determine a pseudo-second order virial coefficient, A_2 , which is used as an indicator for compatibility of the filler and polymer. It is found that A_2 follows the expected behavior with lower values for smaller primary particles indicating that smaller particles are more difficult to mix. A_2 is analogous to the excluded volume and long-range interaction potential for non-equilibrated nanocomposites. The measured values of A_2 can be used to specify repulsive interaction potentials for coarse grain DPD simulations of filler/elastomer systems. In addition, new methods to quantify the filler percolation threshold and filler mesh size as a function of filler concentration are obtained. The results represent a new approach to understanding and predicting dispersion in polymer nanocomposites based on a thermodynamic analogy.

© 2017 Elsevier Ltd. All rights reserved.

1. Introduction

Processed polymers usually consist of multiple immiscible components such as pigments, fillers, and compounding agents. For complex polymeric mixtures an understanding of relative compatibility or dispersibility of the components on a fundamental level is desirable. Such an understanding could help in the design of polymer nanocomposites and in the control and prediction of behavior. For example, reinforcing fillers such as carbon black (CB) and silica are used in rubber products. The reinforcing ability depends on the structure of the fillers, and the interaction between filler particles and the elastomer matrix as well as the processing history. Aggregated fillers can be quantified by the specific surface

area (and the related primary particle size), the degree of graphitization for carbon, and the hydroxyl surface content for silica. A description of filler structure also includes the fractal aggregate structure that allows access to the surface through spatial separation of primary particles. The fractal structure also contributes a static spring modulus to the composite at size scales larger than the filler mesh size for concentrations above the percolation threshold [1]. Aggregates are often clustered in agglomerates that can largely be broken up during the elastomer milling process.

The affinity for a filler/polymer pair is evidenced by their dispersability and their reinforcing properties in elastomer composites. Since fillers are often nanomaterials, standard characterizations of compatibility focus on the specific surface area. The surface area of fillers is usually measured by iodine adsorption (mg/g of filler), nitrogen adsorption (m^2/g of filler), or cetyltrimethylammonium bromide (CTAB) adsorption (m^2/g of filler) [2,3]. The structure of fillers has been quantified using oil absorption (g/100 g of filler) or dibutyl

* Corresponding author.

E-mail address: gbeaucage@gmail.com (G. Beaucage).

phthalate (DBP) absorption (ml/100 g of filler) for CB [2,3], as well as through a variety of surface characterization techniques such as determination of the surface hydroxyl content for silica, and the degree of graphitization for carbon black. In addition, techniques have been applied to study compatibility of filler in the rubber matrix by investigating surface and aggregate structure. Göritz et al. used atomic force microscopy (AFM) and small angle x-ray scattering (SAXS) to study surface structure and fractal dimension of CB [4]. Scanning electron microscopy (SEM) [5] and transmission electron microscopy (TEM) [6] were used to study particle size and morphology of aggregates. Herd et al. [7,8] discovered four types of CB aggregates by TEM: spheroidal, ellipsoidal, linear and branched shapes. Koga et al. investigated hierarchical structure of CB combining techniques of ultra-small angle and small angle scattering of X-rays and neutrons (USAXS, SAXS and USANS) [9]. Abraham et al. introduced a technique of sorption to analyze the compatibility of filler in the rubber matrix by studying transport and diffusion of small molecules through matrix [6].

Silica is the traditional reinforcing filler for polydimethylsiloxane elastomers due to compatibility in chemical structure. Silica was introduced as a reinforcing filler for diene elastomers for tires in the 1990's and showed a lower rolling resistance and higher fuel efficiency compared to carbon black reinforcing filler [2,5]. However, silica is very different compared to CB filled rubbers due to its strong polar and hydrophilic surface. A certain quantity of moisture can be adsorbed on the silica surface and it is difficult to remove. This is especially true of precipitated, colloidal silica and silica gel. Pyrolytic silica has an essentially pristine surface but is rarely used for elastomer reinforcement except for siloxane elastomers. Inter-particle interaction of silica due to hydrogen bonding and Coulombic interactions needs to be considered since it weakens the compatibility of silica and rubber [2].

Several groups have considered the impact of surface energy and interfacial modification on dispersion under non-equilibrium processing conditions [10–14]. Stöckelhuber et al. [10] determined the contact angle and surface energy of fillers and elastomer gums to calculate the free energy of emersion of fillers in elastomers. A negative free energy of immersion favors dispersion, and a positive value favors flocculation. The surface energy was broken into a dispersive energy associated with London's dispersive forces and a polar component associated with polar functional groups. These were determined through measurement of the dynamic contact angle. The free energy of immersion depends on the polar component of the elastomer surface energy and the dependence is associated with chemical surface modification. The work of adhesion for filler in polymer can also be calculated from surface energies. This shows a similar dependence on the polar part of the surface energy of rubbers. A large work of adhesion could be associated with good dispersion and poor flocculation. The difference in work of adhesion between the dispersed and flocculated state is related to the formation of a filler network. Evidence from TEM qualitatively supports the approach.

Stöckelhuber et al. [11] further considered the mechanics of elastomer composites in the framework of surface energies. Stöckelhuber developed a plot of surface energy of the filler versus the polar component of the filler surface energy and proposed regimes within this plot where good wetting and good adhesion of the filler would occur in a given elastomer. This mapping enables filler selection for a specific elastomer. TEM and dynamic mechanical measurements were used to verify the approach.

Natarajan et al. [12] studied siloxane polymers of variable polar surface energy, as described by Stöckelhuber [11], filled with surface modified colloidal silica of variable polarity. A comparison was made of the Stöckelhuber plot [11] with TEM micrographs and the glass transition temperature which is sensitive to surface

interactions between polymer and filler. The average cluster radius and the average intercluster distance were determined from the micrographs. These showed expected trends in the work of adhesion. Shifts in the glass transition also correlated with a function of the work of adhesion.

Hassinger et al. [13] extended the work of Natarajan et al. towards prediction of dispersion under non-equilibrium processing conditions. They coupled the ratio of the work of adhesion between filler/polymer and filler/filler, developed by Stöckelhuber et al. [10], and a calculated mixing energy to correlate with the interfacial area calculated from TEM images. A model was proposed that correlates the interfacial area reflecting dispersion and a combined term involving the work of adhesion ratio and the calculated mixing energy. Good correlations are found between these parameters.

The prior work based on interfacial energy has had significant success. Coupling of mixing energy with interfacial energies is an appealing approach [13]. However, for the most part this approach has been applied at concentrations below the percolation concentration where TEM analysis and verification is appropriate. The expected primary particle size dependence based solely on surface energy would predict that small particles with high specific surface area that display favorable surface energies should disperse better than larger particles. However, the opposite is often the case for commercial reinforced elastomers above the percolation threshold in the semi-dilute regime for fillers. Further, the measured surface energy is an equilibrium property that reflects local interactions such as those that affect the interfacial T_g [14,15]. These short-range interactions are often attractive and lead to aggregation in many nanocomposites such as pigment dispersions. Despite short-range aggregation that reflects disadvantageous interfacial energies it is still common to disperse aggregates at larger scales through mechanical mixing. A complementary approach is to consider, in addition to short-range interactions that can lead to aggregation, long-range interactions that lead to dispersion based on excluded volume. This approach can lead to the prediction of properties that can not be accessed using short-range surface interactions. For instance, long-range interactions may be responsible for the filler aggregate percolation threshold or overlap concentration and may correlate with the filler network mesh size. Features such as the filler percolation concentration and filler network mesh size may influence the properties of nanocomposites, especially those that are difficult to describe based on short-range interactions and that are related to the emergent structure in semi-dilute concentrations of filler.

In this paper an analogy is made between thermally driven dispersion in colloidal mixtures and mechanically driven dispersion, particularly in aggregated nanocomposites such as carbon black and silica in elastomers. In this pseudo-thermodynamic approach it is possible to obtain an effective long-range repulsive potential that can be used to describe the complex structural result of the interplay between excluded volume, surface energy and mixing kinetics for nanostructures that display an emergent, kinetically frozen, and disperse filler aggregate network structure such as in commercial reinforced elastomers and pigment dispersions in inks, paints and plastics.

The compatibility of colloidal solutions such as mixtures of miscible polymers, solutions of low molecular weight organics and inorganics, and biomolecules is often quantified using the virial expansion to describe the concentration dependence of the osmotic pressure. This approach assumes that molecular and nanoscale motion and the associated dispersion is governed by thermally driven diffusion with a molecular energy of $k_B T$. Elastomer/reinforcing filler compounds have not been considered equilibrium colloidal mixtures since the materials are highly viscous or solid networks so it is difficult to imagine thermally driven motion

leading to dispersion of reinforcing filler aggregates in an elastomer composite. However, there is precedence to the use of the virial expansion in viscous systems such as in polymer melts where Flory–Huggins theory is applied. The virial coefficient is also used in native state protein solutions where rigid protein nanostructures are considered. The quantification of “compatibility” using a “pseudo-virial” approach may be of value in reinforced elastomer systems (and a number of other similar systems) where an analogy can be considered between randomly placed filler aggregates dispersed in the milling process and randomly placed molecules dispersed by thermal motion. In this analogy, it is assumed that the mixture has reached a stable state of dispersion related to the processing history, interfacial energies, filler structure, and matrix viscosity. In this pseudo-thermodynamic approach, processing time, accumulated strain, matrix viscosity all may have some equivalence to temperature in a true thermodynamic system. That is, the “compatibility” for a given binary compound could change with processing conditions, in addition to filler and matrix type, since an analogy to equilibrium is considered and not a true thermal equilibrium.

In colloidal mixtures it is common to consider the miscibility of a binary system in terms of the second virial coefficient [16–18]. For instance protein precipitation from solution in the process of protein crystallization has been predicted using the second virial coefficient. The virial expansion is used to describe deviations from ideal osmotic pressure conditions, $\pi = \phi_{num}RT$, using a power series expansion [19],

$$\frac{\pi}{kT} = \phi_{num} + B_2\phi_{num}^2 + B_3\phi_{num}^3 + \dots \quad (1)$$

where ϕ_{num} is the number density of particles or molecules. B_2 reflects the enhancement of osmotic pressure due to binary interactions of a colloid in a matrix in terms of the thermal energy, $k_B T$. B_2 is related to an integral of the interaction energy between particles, as described below. Such a binary interaction energy can be used as an input to computer simulations of polymer/filler mixing. B_2 could also be used to quantify filler/polymer interactions in prediction of mechanical and dynamic mechanical performance. If trends in B_2 can be determined as a function of, for example, particle size or chemical composition of an elastomer matrix or surface-active additives, then these values could be used to predict the performance of new compositions for enhanced performance. In this study a binary compound could be considered a matrix phase composed of a polymer and miscible additives such as oil/plasticizer and processing aids mixed with an immiscible additive such as a reinforcing filler.

A parallel definition of the second virial coefficient using the mass density concentration, ϕ_{mass} , rather than the number density concentration, ϕ_{num} , is possible,

$$\frac{\pi}{RT} = \phi_{mass}/M + A_2\phi_{mass}^2 + A_3\phi_{mass}^3 + \dots \quad (2)$$

where M is the molecular weight of a particle. $\phi_{mass} = M\phi_{num}/N_a$. N_a is Avogadro's number, and $A_2 = B_2N_a/M^2$, following Bonneté et al. [19]. B_2 has units of $\text{cm}^3/\text{particle}$, and A_2 has units of mole cm^3/g^2 .

B_2 is related to the binary interaction potential for particles, $U(r)$, by,

$$B_2 = 2\pi \int_0^\sigma r^2 \left(1 - e^{-U(r)/kT}\right) dr \quad (3)$$

If a hard core potential is assumed, then the hard core radius, σ_{HC} , is given by,

$$\sigma_{HC} = \left(\frac{3A_2M^2}{2\pi N_a}\right)^{1/3} = \left(\frac{3B_2}{2\pi}\right)^{1/3} \quad (4)$$

σ_{HC} should be a size scale on the order of the size of an aggregate so this serves as a check for the validity of the second virial coefficient.

The second virial coefficient can be used to predict stability and compatibility of elastomer/filler systems, especially when coupled with coarse grain DPD (dissipative particle dynamics) simulations. A typical repulsive potential for a DPD system is of the form [20],

$$\frac{U(r)}{kT} = \frac{A}{2} \left[1 - \left(\frac{r}{\sigma}\right)\right]^2 \quad (5)$$

where σ is the diameter of the aggregates, in this paper the end to end distance R_{eted} for the aggregate is used for σ . A is a dimensionless binary repulsive amplitude that can be defined for particle interactions that are at play in a specific situation. Equation (5) can be used in equation (3) and numerically solved for “ A ” using B_2 . “ A ” might be used to simulate the behavior of a filler in an elastomer matrix to determine the segregation of filler in a polymer compound, for example.

2. Scattering to determine the second virial coefficient

Ultra small-angle X-ray scattering data from carbon black and silica reinforced elastomer composites was fitted using the unified scattering function [21–23]. For the carbon black samples, first a unified function for the mass fractal aggregates was used with three structural levels,

$$I_0(q) = \sum_0^2 \left\{ G_i e^{\left(\frac{-q^2 R_{gi}^2}{3}\right)} + e^{\left(\frac{-q^2 R_{gi+1}^2}{3}\right)} B_i (q_i^*)^{-P_i} \right\} \quad (6)$$

where $q^*_i = q/[\text{erf}(qR_{gi}/(6)^{1/2})]^3$, level 0 pertains to a graphitic layer, level 1 to the primary particles and level 2 the aggregate structure. Level 0 does not exist for silica. The subscripted “ I_0 ” in equation (6) refers to dilute conditions or isolated fractal aggregates in the absence of screening, described below. For each structural level the unified function uses four parameters to describe a Guinier and a power-law decay regime. For the smallest scale, at highest q , a graphitic layer, level 0, can be observed with a power-law decay of -2 slope for 2d graphitic layers. These layers typically display a lateral dimension of about 15 Å. Level 1 pertains to the primary particles of the aggregates, which have a typical radius of gyration of about 170 Å. The primary particles form aggregates, level 2, with a typical mass fractal dimension of about 2.1, the aggregates having a typical radius of gyration of about 2200 Å. For silica filled samples the graphitic surface layer, level 0, is not used.

From the scattering fit parameters several calculated parameters can be obtained. For the primary particles, the Sauter mean diameter or equivalent spherical diameter, d_p , a polydispersity index, PDI , the log-normal geometric standard deviation, σ_g , and the geometric mean value of size, μ , are obtained. For the fractal portion of the scattering curve the minimum dimension, d_{min} , connectivity dimension, c , mole fraction branching, ϕ_{Br} , degree of aggregation, z , aggregate polydispersity, C_p , number of branch per aggregate, n_{br} , and average branch length, z_{br} , can be obtained (among other parameters) [22–28]. The end-to-end distance, used for σ in equation (5), can be calculated from,

$$R_{eted} \sim d_p p^{1/d_{min}} \quad (7)$$

The interaction between filler and elastomer can be modeled using the random phase approximation, RPA, following Vogtt et al. [29–31],

$$\frac{\phi_w}{I(q)} = \frac{\phi_w}{I_0(q)} + v\phi_w \quad (8)$$

where ϕ_w is the weight fraction, and v is related to the second virial coefficient by Refs. [29,32],

$$A_2 = \left(\frac{v \langle \Delta \rho^2 \rangle}{2N_a \rho_{particle}^2} \right) \quad (9)$$

$$B_2 = M^2 A_2 / N_a = \left[z \rho_{particle} \left(4\pi (d_p/2)^3 / 3 \right) \right]^2 A_2 / N_a$$

Fig. 1 is a schematic of the effect of $v\phi_w$ in equations (6)–(9) on the scattering pattern as well as a cartoon of how the overlap of aggregates (shown as a chain structure for simplicity) can lead to the loss of resolution of an individual chain aggregate for concentrations above the overlap concentration. The mesh size, a size-scale where the structure of the first cartoon can be resolved in the more concentrated samples becomes smaller with increasing concentration. This can be observed as the point in $\log q$ where the horizontal line crosses the dilute I/ϕ curve. The local percolation threshold or overlap concentration is the concentration where the local concentration matches the concentration within an aggregate. This is a concentration between the first two cartoons in Fig. 1 and a point where the dashed horizontal line just meets the scattering curve. The percolation threshold on the nanoscale may not agree with the bulk percolation threshold such as measured by conductivity in carbon black dispersions.

In addition to the mass fractal structure and screening (equations (6) and (8)), Fig. 2 shows the effect on scattering of the formation of a super-structure composed of fractal aggregates that

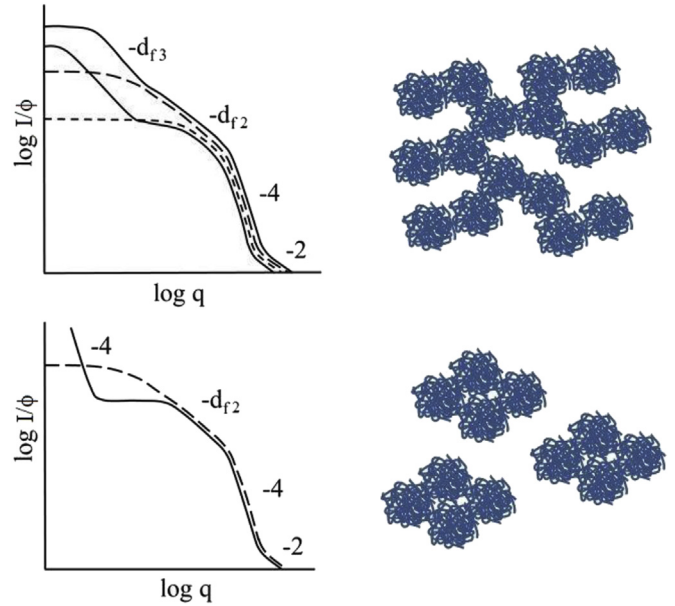


Fig. 2. Schematics of formation of agglomerate superstructure in the concentrated regime from the third structure in Fig. 1. Top: fractal super structure. Bottom: domain super structure. The large-dashed curves reflect the dilute condition, $I_0(q)/\phi_0$. The small dashed curve in the top graph is a screened curve in the semi-dilute regime in the absence of agglomeration at low- q similar to the third structure in Fig. 1. The solid curves reflect the presence of agglomerates at low- q and screening at intermediate- q .

agglomerate either into a mass-fractal structure or into 3D-domains. For the carbon black studied here the super-structure displays a fractal-like mass distribution, but only the power-law decay from these agglomerates of aggregates is observed with a fractal dimension of about 2.8. This agglomerate structure can be accommodated as a fourth structural level using the unified approach,

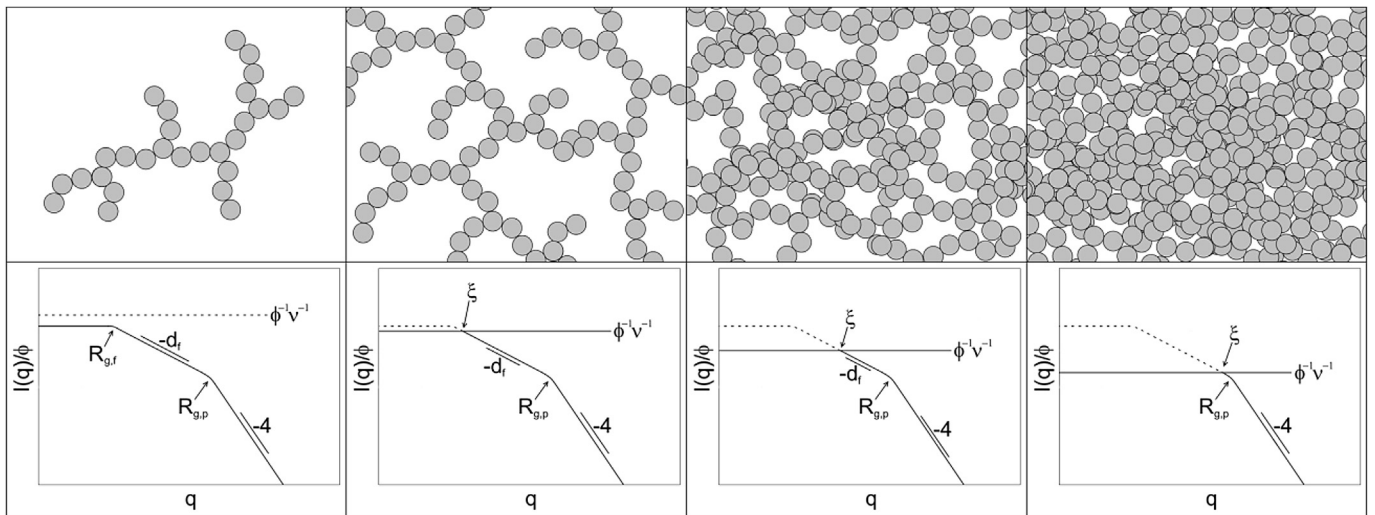


Fig. 1. Schematic of the screening effect and scattering in the semi-dilute regime. As concentration increases (going from left to right), the filler aggregates begin to overlap and larger features become obscured due to screening. The solid line in the graphs is the observed scattering, the dotted line in the right three graphs reflects the screened scattering from the dilute condition, $I_0(q)/\phi_0$. Instead of aggregate size, the largest observable structural feature in the semi-dilute regime is the mesh size, ξ . At higher concentrations, the mesh size continues to decrease and information about larger structural features is lost. The model does not include structural correlations that would lead to the contribution of a structure factor in scattering.

$$I_{Net}(q) = I(q) + e\left(\frac{-q^2 R_g^2}{3}\right) B_3 q^{-P_3} \quad (10)$$

where B_3 is the power-law prefactor for the lowest- q agglomerate structure. The agglomerate scattering is experimentally observed to be independent of the screening effect of equation (8) since the agglomerates are dilute at large scales.

The agglomerate structure might be associated with bulk percolation of the carbon structure that is measured by conductivity. A local percolation exists where the effects of screening are first observed between the first two frames of Fig. 1. In a simplified view this local percolation (Fig. 1) might impact the dynamic mechanical spectrum, while the agglomerate percolation in Fig. 2 might be expected to impact the static bulk properties. X-ray tomographic images of the agglomerate structure were recently reported by Song et al. [33].

3. Experimental

Samples were milled in a 50 g Brabender mixer at 130 °C with a rotor speed of 60 rpm for 6 min until the torque versus time curve had dropped from a peak value and reached a plateau. Table 1 shows the 10 sample types for two elastomers filled with five fillers. Each type was studied with four concentrations of 1, 5.6, 15.1 and 29.9 wt %. 140ND is Diene 140ND from Firestone Polymer [34] while B45 is Buna CB45, Lanxess [35] (B45 is used rather than CB45 to avoid confusion with carbon black). B45 has a lower *cis*-1,4 content (38% *cis*-1,4 content, Mooney Viscosity 45 MU) compared with 140ND (96% *cis*-1,4 content, Mooney Viscosity 42 MU). The polyisoprene sample, labeled PI, was obtained from Sigma Aldrich ($M_w \sim 38,000$ g/mole, natural origin, viscosity 350 P or approximately 66 MU (37 °C), Stock number 431257).

Nanoparticles were used as manufactured with no surface treatment. SiO₂ 190 is HiSil 190G from PPG with a N₂ surface area of 195 m²/g ($d_p = 14.0$ nm), and an oil absorption of 210 ml/100 g, pH 7. HiSil 190G is precipitated amorphous silica and is typically used in tire compounds. SiO₂ 130 is Aerosil 130 from Evonik. Aerosil 130 is fumed silica with a specific surface area of 130 m²/g ($d_p = 21.0$ nm) and a pH of 3.7–4.5. It is not typically used in tire compounds. For the silica powders the Sauter mean diameter, $d_p = 6$ V/S, agrees well between gas adsorption, and X-ray scattering measurements on powders and nanocomposites discussed below. The precipitated silica, HiSil 190G, has significant hydroxyl surface content. The fumed silica, Aerosil 130, has much lower surface hydroxyl content.

All three of the carbon blacks are commonly used in tire compounds. CB110 is also called N110 and sold as Vulcan V8 by Cabot Corporation. Vulcan V8 has an oil absorption number of 113 ml/100 g and a specific surface area of 123 m²/g ($d_p = 25.7$ nm). CB330 is also called N330 and is sold as Vulcan V3 by Cabot Corporation. Vulcan V3 has an oil absorption number of 102 ml/100 g and a specific surface area of 76 m²/g ($d_p = 41.6$ nm). CRX is CRX 2002 produced by Cabot Corporation. CRX 2002 has an oil absorption of about 140 ml/100 g and a specific surface area of about 140 m²/g ($d_p = 22.6$ nm). The equivalent spherical diameter of the primary

particles, d_p , for Vulcan V8 in powder (X-ray and gas adsorption) agrees with X-ray measurements on the nanocomposites as discussed below. For Vulcan 3, the nanocomposite primary particle diameter is about half the value for powder indicating breakup of primary particle clusters when milled with rubber. For CRX 2002 the primary particles also appear to breakup on milling with the elastomers. Koga et al. [36] extensively reported on the breakup of primary particle clusters on milling with an elastomer using a carbon black similar to CB330 and agreeing with the observed behavior of CB330 and CX 2002. The X-ray measured nanocomposite primary particle d_p 's are used in the correlations and analysis below.

Measurements were performed at the Advanced Photon Source, Argonne National Laboratory, using the Ultra-Small-Angle X-ray Scattering (USAXS) facility located at the 9 ID beamline, station C. The instrument is designed and operated by Jan Ilavsky [37].

Scanning transmission electron microscopy was performed on ~80 nm thick sections of nanocomposites obtained at a temperature much below the glass transition temperature of the sample using a cryo-ultramicrotome and collected onto 200-mesh carbon-coated, copper support grids. Images were obtained using a transmission electron microscope operating in STEM mode with an accelerating voltage of 25 kV and an emission current of 10 μA.

4. Results

Fig. 3 shows plots of the three one percent CB samples, B45-CB330_1, PI-CB330_1, 140ND-CB330_1 and the fit for B45-CB330_1. The pure polymer scattering has been subtracted from

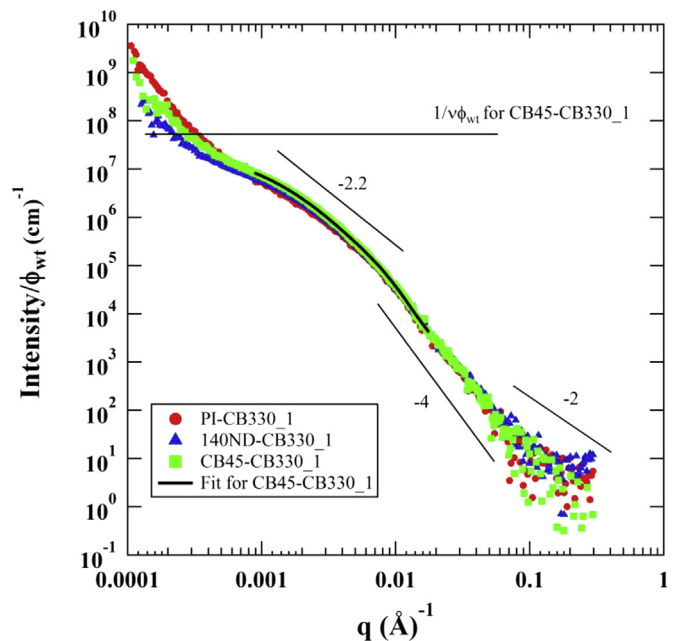


Fig. 3. Plots of the three 1 wt % carbon black 330 reinforced polymers. A two level unified fit to the B45-CB330_1 samples is shown. The scattering curves are scaled to match the 140ND-CB330_1 curve at high q .

Table 1
USAXS sample names (each with four concentrations 1, 5.6, 15.1, and 29.9 wt %).

	SiO ₂ 130	SiO ₂ 190	CB 110	CB 330	CRX 2002
B45	B45-Si130	B45-Si190	B45-CB110	B45-CB330	B45-CRX
140ND	140ND-Si130	140ND-Si190	140ND-CB110	140ND-CB330	140ND-CRX
PI	PI-Si130	PI-Si190	PI-CB110	PI-CB330	PI-CRX

Table 2

Structural fit parameters for the dilute 1% carbon black and silica samples. (Standard deviations, propagated from the statistical error in the data, are given in the [supplemental material](#). Significant digits indicate the order of the standard deviation.)

	$G_1, \text{cm}^{-1} 10^5$	$R_{g1}, \text{\AA}$	$B_1, \text{cm}^{-1} \text{\AA}^{-P_1} 10^{-4}$	P_1	$G_2, \text{cm}^{-1} 10^6$	$R_{g2}, \text{\AA}$	$B_2, \text{cm}^{-1} \text{\AA}^{-P_2}$	P_2
B45-Si130_1	2.10	256	15.0	4	13.0	1180	0.258	2.6
PI-Si130_1	2.60	280	11.7	4	22.2	1180	0.628	2.6
140ND-Si130_1	2.53	257	19.0	4	17.0	1180	0.521	2.58
B45-Si190_1	0.184	86.1	11.4	4	13.2	1300	0.251	2.52
PI-Si190_1	0.144	86.7	7.32	4	13.2	1200	0.14	2.68
140ND-Si190_1	0.178	86	20.2	4	8.27	1060	0.17	2.61
B45-CB110_1	3.02	313	4.60	4	6.65	1513	1.31	2.27
PI-CB110_1	2.35	293	4.25	4	4.5	1420	0.631	2.35
140ND-CB110_1	2.75	298	4.56	4	4.05	1380	0.784	2.32
B45-CB330_1	0.172	163	2.82	4	12.5	1750	3.56	2.15
PI-CB330_1	0.256	190	1.28	4	15.8	2160	13.7	1.9
140ND-CB330_1	0.172	163	2.82	4	12.5	1750	3.56	2.15
B45-CRX_1	0.182	179	4.8	4	10.2	1650	2.06	2.2
PI-CRX_1	0.170	179	5.0	4	20.5	2880	8.04	2
140ND-CRX_1	0.176	179	4.9	4	21.0	2880	7.2	2

Table 3

Calculated structural parameters for the dilute filler samples from the first and second structural levels (primary particles and aggregates). (Standard deviations, propagated from the statistical error in the data, are given in the [supplemental material](#).)

	z	d_{min}	c	d_f	C_p	p	R_{eted}, nm	n_{br}	d_p, nm	PDI	σ_g	μ, nm
B45-Si130_1	61.9	1.40	1.86	2.60	1.53	9.2	92.9	6.92	19.0	19.4	1.64	133
PI-Si130_1	85.4	1.85	1.41	2.60	1.65	23.7	118	1.12	21.3	17.1	1.63	155
140ND-Si130_1	67.2	1.80	1.43	2.58	1.60	18.8	96.6	1.28	18.9	20.0	1.65	131
B45-Si190_1	717	1.28	1.96	2.52	1.15	28.2	221	68.8	16.3	2.11	1.28	149
PI-Si190_1	917	1.41	1.90	2.68	1.50	36.2	236	43.3	18.5	1.77	1.24	164
140ND-Si190_1	465	1.35	1.93	2.61	1.30	24.0	119	35.9	11.3	3.84	1.40	107
B45-CB110_1	22.0	1.96	1.16	2.27	1.80	14.4	110	0.08	28.3	9.00	1.53	245
PI-CB110_1	19.2	1.98	1.19	2.35	1.98	12.1	96.0	0.1	27.3	8.27	1.52	241
140ND-CB110_1	14.7	1.99	1.16	2.32	1.98	10.0	89.2	0.06	28.0	8.07	1.52	248
B45-CB330_1	324	1.83	1.21	2.20	1.60	123	253	0.7	18.3	8.37	1.52	162
PI-CB330_1	617	1.18	1.61	1.90	1.50	54.1	715	77.9	24.3	4.02	1.41	231
140ND-CB330_1	727	1.69	1.27	2.15	1.60	178	343	2.62	16.0	7.16	1.50	145
B45-CRX_1	560	1.53	1.43	2.20	1.60	81.5	243	8.57	13.7	16.6	1.62	101
PI-CRX_1	1210	1.86	1.08	2.00	1.75	736	466	0.13	13.4	18.6	1.64	94.8
140ND-CRX_1	1010	1.77	1.13	2.00	1.60	456	852	0.76	13.5	16.0	1.55	97

the nanocomposite samples and the resulting intensity is normalized by filler concentration. [Tables 2 and 3](#) show the fit and calculated results for the 15 one percent samples listed in [Table 1](#).

The scattering pattern at 1 wt % reflects the structure of CB aggregates. The carbon black includes four levels of structure. Level 0 pertains to the graphitic structure observed above $q = 0.02 \text{\AA}^{-1}$. The graphitic level displays a power-law -2 for the 2d structure. From about 0.008 to 0.02\AA^{-1} the primary particle structure is observed, level 1. The data was fit assuming that this level displays smooth, sharp surfaces indicated by a power-law decay of -4 slope following Porod's law. Koga et al. [36] extensively discussed the origin of details in this region reflecting the internal structure of particle clusters that can form the primary particles for some carbon blacks. The data in [Fig. 3](#) does not show sufficient resolution for such an analysis. Also, the CB110 sample and the silica samples do not display discrepancies between the powder (gas absorption and scattering) and nanocomposite (scattering) d_p indicating that they might not contain complex primary particle clusters described by Koga for a carbon black similar to CB330 [36]. For consistency in the data analysis and reduction and within the accuracy of the data it is assumed here that the particles display smooth sharp interfaces so that an equivalent spherical diameter, d_p , can be directly obtained from Porod's law for comparison of different nanocomposites. It

would be interesting to further explore the impact of primary particle breakup [36] on the virial description of dispersion.

From 0.0008 to 0.008\AA^{-1} the fractal aggregate, level 2, is observed with a power-law decay reflecting $-d_f$ for the aggregate. At the lowest q , a steep, power-law decay is observed which reflects surface scattering from a large-scale structure of agglomerates of CB aggregates or from defects in the samples. The power-law decay varies between mass fractal and domain structures, [Fig. 2](#). Only scattering from the dispersed aggregates component of the structure is of interest for the determination of A_2 . Screening in equation (8) only effects levels 0 to 2 since the large-scale super-structure, level 3, is under dilute conditions, as implied in equation (10). At higher concentrations, fits to only levels 1 to 2 are considered to simplify the fits since the graphitic substructure of CB primary particles has no impact on screening or the scattering below about 0.05\AA^{-1} .

[Fig. 3](#) shows that for the dilute 1% filled samples, a given filler displays the same q dependence regardless of the matrix polymer. This indicates that the structure does not significantly change on the nano-scale when milled with different polymers. The scattering curves have been scaled to the 140ND-CB330_1 curve since there are differences in absolute intensity due to differences in contrast. Sample PI-CB330_1 shows a different primary particle R_{g1}

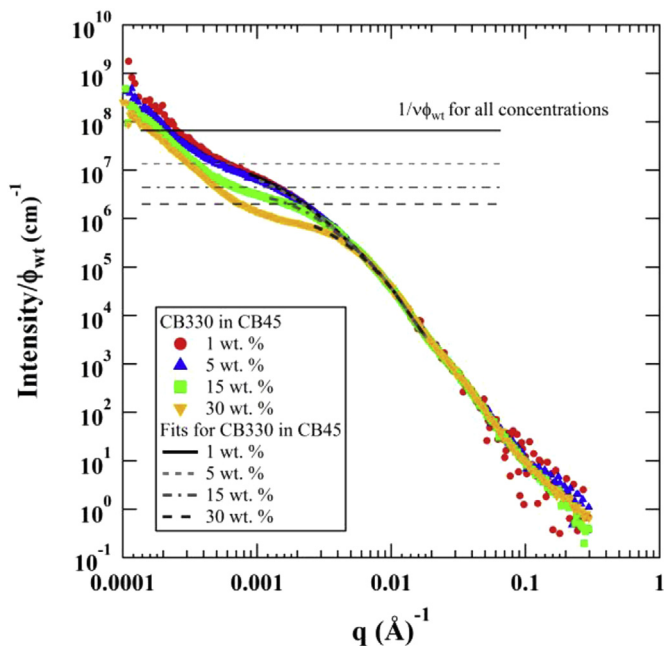


Fig. 4. Log I/ϕ versus log q for B45-CB330. A fit for the 1% sample is used as the basis for fits from 1 to 30% samples using one parameter, ν , in equation (8). Intensity at intermediate- q drops with concentration following equation (8). Values of $1/(\nu\phi_{wt})$ are also plotted for comparison with the scattering curve, $\nu = 1.35 \times 10^{-6}$ cm.

compared to the other two CB330 1% samples in Table 1. B45-CRX_1 displays a different aggregate structure as reflected in R_{g2} compared to the other two CRX 1% samples. This will be discussed further below.

Fig. 4 shows scattering from the concentration series for the B45-CB330 samples. As concentrations increase, the high- q part of the concentration-reduced scattering curves remains unchanged in a log-log plot of I/ϕ_{wt} versus q . At intermediate- q I/ϕ_{wt} drops due to the screening effect of equation (8). The rate of decrease in I/ϕ_{wt} with concentration in this intermediate q -range is an indicator of how well the filler is dispersed in the elastomer. If the filler were in a thermodynamically-equilibrated colloidal dispersion this diminution of I/ϕ_{wt} would be directly related to the second virial coefficient (or the excluded volume and χ -parameter for polymer blends). For filler in an elastomer, thermodynamic mixing governed by $k_B T$ does not exist. In its place we have random dispersion caused by mechanical milling. For this case, a processing dependence is expected to the pseudo-thermodynamic property that we observe in the reduction in I/ϕ_{wt} with concentration for filled elastomers.

In order to obtain values for ν in Fig. 4, fits were performed on the lowest concentration samples, B45-CB330_1 setting $\nu\phi_{wt}$ in equation (8) to 0. Under the assumption that the carbon black structure is not sensitive to concentration, fits using the structural parameters from the 1% sample, listed in Table 2, were done for the each higher concentration sample, B45-CB330_5, B45-CB330_15, and B45-CB330_30, fitting only ν . Verification that $\nu\phi_{wt}$ for the 1% samples does not impact the scattered intensity is seen when the value of $1/(\nu\phi_{wt})$ is far larger than the scattered intensity for the fractal part of the dilute curve as seen in Figs. 3 and 4 for the 1% samples (solid line in Fig. 4). This indicates that the 1% samples are dilute, that is the sample is well below the overlap concentration or local percolation threshold for the filler aggregates. Fig. 4 shows the impact of $\nu\phi_{wt}$ for the entire concentration series for B45.

The pseudo-second order virial coefficient, A_2 , in binary milled compounds is obtained from the rate in concentration of

dampening (reduction in intensity) of the mid- q data in Fig. 4. The larger A_2 , the greater the rate of dampening in concentration and the better dispersed the filler/elastomer/compounding agent mixture. Table 4 shows the values of ν from equation (8) and the calculated A_2 for the three polymers, B45, PI, and 140ND for each of the five fillers, Si130, Si190, CB110, CB330, and CRX. A_2 is converted to B_2 using the mean value of d_p , Table 4. The hard-core diameter, σ_{HC} , is calculated from B_2 , Table 4. Finally, equations (5) and (3) are used to determine the unitless short-range potential amplitude “A” using the mean value of the chain end-to-end distance, $R_{eted} = \langle d_p \rangle p^{1/d_{min}}$, for σ . In Tables 4 and 5 “S” indicates the presence of a prominent structure factor leading to a peak in the scattering data and making the virial approach impossible. This is observed in silica samples where primary particles can carry a charge as discussed below. The analysis failed for one of the carbon black samples, PI-CB330. This is associated with the larger primary particle and aggregate size in Table 2 compared to the other two CB330 samples.

Fig. 5a shows an example where the fractal aggregate of Si190 displays structural correlations for higher concentration blends in B45. CB330 doesn't show such correlations in Fig. 5b. Note that the higher concentration curves have a higher normalized intensity at some intermediate q -values compared to the lower concentration curves, which is incompatible with equation (8).

The second virial coefficient is an indication of miscibility with larger values indicating greater affinity in a binary mixture. Similarly the pseudo-second virial coefficient indicates the goodness of dispersion. It is commonly observed that mixing of fine particulate fillers is more difficult than coarse fillers. So it is expected that a monotonic relationship between nanoparticle size and the pseudo- A_2 might exist for matched processing conditions. Fig. 6 shows close to a linear relationship between A_2 and the primary particle Sauter mean diameter, d_p , for various nanoparticulate carbon black fillers. The trend agrees with the expectation that smaller nanoparticles display lower compatibility. The symbols are grouped into polymer type, circles B45, squares 140ND, and triangles PI. The open symbols are for silica fillers and the closed symbols for carbon black. Silica fillers display larger A_2 's compared to carbon black indicating better dispersion for the same primary particle size.

Of the three types of polymers polybutadiene 140ND with high cis 1,4 (squares in Fig. 6) displays consistently better dispersion. polyisoprene is better dispersed compared to B45 with low cis 1,4 and high vinyl 1,2 units. Further, the intercept of the trend lines in Fig. 6 at $d_p = 0$ reflects the pseudo- A_2 value for a particle completely composed of surface, $S/V \sim 1/d_p = \infty$. This intercept is positive for the high cis 1,4 polybutadiene 140ND, close to 0 for PI, and negative for the low cis 1,4, high vinyl 1,2 polybutadiene B45, indicating surface attributes that encourage mixing in 140ND, but which are neutral for PI and favor demixing for B45. For B45 a minimum Sauter mean diameter of about 3 nm is the smallest particle that can be dispersed under these processing conditions. Pires et al. [38] similarly found that high cis 1,4 polybutadiene displayed better nanocomposite dispersion compared to low cis 1,4 polybutadiene. The slope of A_2 versus particle size is similar for the three polymers in composites with carbon black. The silica A_2 values are consistently higher than carbon black indicating better dispersion for silica compared to carbon black of similar primary particle size.

The precipitated silica, HiSil 190G, has significant hydroxyl surface content, while the fumed silica, Aerosil 130, has much lower surface hydroxyl content. HiSil 190G displayed structuring (a structure factor) in polyisoprene, while the fumed silica, Aerosil 190, displayed structuring in both of the polybutadienes (high cis 1,4 and low cis 1,4-high vinyl) but not in polyisoprene. There doesn't appear to be a trend in A_2 values between the two types of silica, but only three of the six samples gave results for A_2 due to structuring.

Table 4

Values of ν and A_2 from equations (8) and (9). B_2 calculated from A_2 , σ_{HC} from equation (4), and “A” from equations (3) and (5) using $\sigma = \langle R_{eted} \rangle$ from Table 3. (S indicates the presence of a structure factor that interferes with the analysis.)^a

	ν , 10^{-6} cm	A_2 , 10^{-9} mol cm ³ /g ²	B_2 , 10^{-14} cm ³ /Aggregate	σ_{HC} , nm	A (Eqn. (5))
B45-Si130	1.7 ± 0.3	3.2 ± 0.5	0.047	61.4	9.31
PI-Si130	S				
140ND-Si130	2.4 ± 0.7	5 ± 1	0.073	71.4	16.9
B45-Si190	S				
PI-Si190	1.9 ± 0.2	3.4 ± 0.3	9	354	–
140ND-Si190	S				
B45-CB110	3 ± 1	4 ± 1	0.053	63.9	5.23
PI-CB110	3 ± 1	4 ± 2	0.033	54.9	4.78
140ND-CB110	3.4 ± 0.4	4.6 ± 0.6	0.03	52.8	5.68
B45-CB330	1 ± 1	2 ± 1	0.43	129	3.1
PI-CB330	(0.9 ± 0.4)	(1.1 ± 0.5)	(5.1)	(294)	(1.47)
140ND-CB330	2.2 ± 0.5	3.0 ± 0.7	1.6	199	5.19
B45-CRX	1.09 ± 0.08	1.5 ± 0.1	0.18	96.9	1.31
PI-CRX	1.5 ± 0.6	1.9 ± 0.8	0.96	168	0.969
140ND-CRX	2 ± 1	3 ± 2	0.93	166	0.145

^a A_2 is the mass-based pseudo-second virial coefficient, ν is a scattering coefficient proportional to A_2 , B_2 is the number-based second order virial coefficient, σ_{HC} is the hard-core radius, “A” is the unitless magnitude of the potential function given in equation (5). PI-CB330 had a problem with primary particle size determination as mentioned in the text so the value is not used in Fig. 6. Values in the table are rounded to the accuracy of the propagated error.

Table 5

Percolation concentrations and mesh size of CB and silica in different polymers. (S indicates the presence of a structure factor that interferes with the analysis.)

	vol. % at percolation using G_2	wt. % at percolation using G_2	mesh size (nm) for 15 wt% sample	mesh size (nm) for 30 wt% sample
B45-Si130	–	–	–	–
PI-Si130	S	S	–	–
140ND-Si130	2.4	5.73	264	–
B45-Si190	S	S	–	–
PI-Si190	4.0	9.25	359	270
140ND-Si190	S	S	–	–
B45-CB110	5.8	11.43	442	275
PI-CB110	7.6	14.77	494	308
140ND-CB110	7.3	14.30	449	282
B45-CB330	4.5	9.13	476	316
PI-CB330	–	–	–	–
140ND-CB330	3.6	7.31	400	270
B45-CRX	–	–	–	–
PI-CRX	3.3	6.67	487	338
140ND-CRX	2.6	5.26	458	317

Fig. 7 demonstrates the graphical determination of the short-range potential amplitude “A” from equation (5) using the measured B_2 value and R_{eted} from Tables 3 and 4 respectively. In Fig. 7, the vertical dashed lines are the experimentally calculated B_2 values shown in Table 4. The intersection of the vertical line and the calculated curve provides the graphically determined value for “A” which can be further used to define the interaction potential in equation (5) (The values in Table 4 were determined using a computer program that follows this graphical procedure.). This potential is useful for coarse grain simulations. For two samples, PI-Si190 and 140ND-CRX, the measured B_2 value was above the calculated curve so that an intersection did not exist. This might be related to the large aggregate size making resolution of the actual aggregate size difficult since the size approaches the instrumental limit.

The concentration series shown in Fig. 4 can be used to determine the overlap concentration for the aggregates, which is a type of local aggregate percolation threshold. The overlap concentration is the lowest value of concentration where $1/(\nu\phi)$ will impact the dilute $l(q)/\phi$ curve for the aggregate structural level. That is, the ϕ value where $1/(\nu\phi) = G_2$ from Table 2. Table 5 lists percolation concentrations of CB and silica in three polymers calculated in this way.

The percolation threshold concentration of carbon black filled samples is usually measured by bulk conductivity and we expect to find a higher concentration on the order of 25–30 wt percent using conductivity [39]. The difference between these two measures of percolation threshold may pertain to differences in the measurements. A conductivity measurement quantifies the first point where a conductive pathway exists across millimeters of sample. The scattering overlap concentration reflects local percolation of the structure. Micrographs of the filled samples in Fig. 8 show such local percolation at about 10 wt percent in the case of N330 carbon black in B45. From the perspective of dynamic mechanical properties, it may be the local percolation at the size scale of the filler network that dominates the mechanical behavior.

The percolation threshold (overlap) concentration is 9.13 wt percent from USAXS, close to that observed in Fig. 8c. It can be seen that the overlap concentration or scattering percolation threshold concentration refers to the first local clustering of the aggregates on the order of five aggregates. For the carbon black N330 sample, the Sauter mean diameter is 18.3 nm, approximately one third of the distance between two scale markers. This seems to agree reasonably well with the micrographs so that the primary particles from

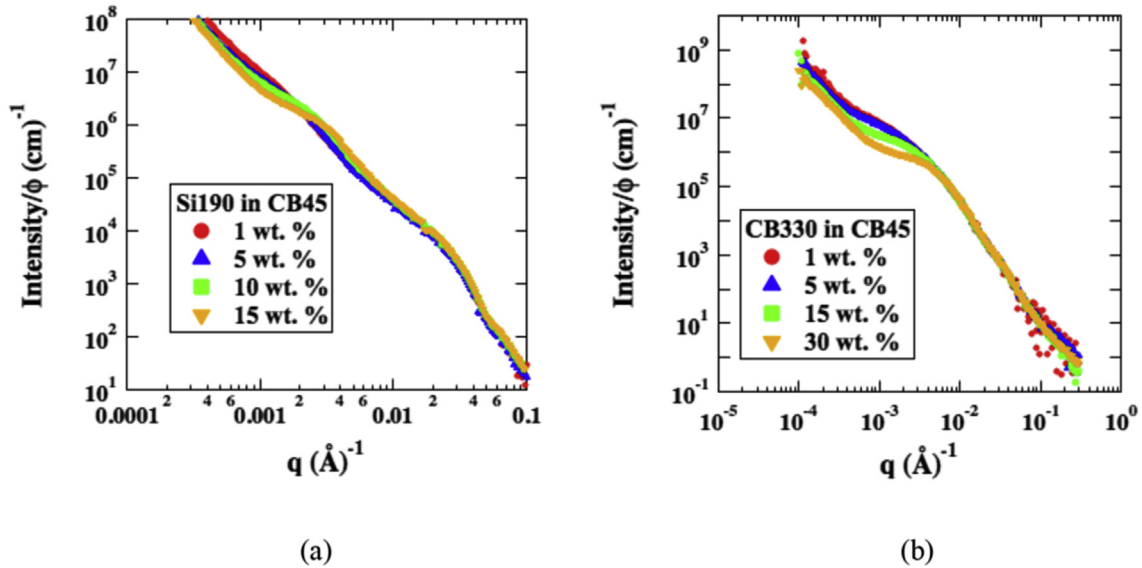


Fig. 5. a) Sample displaying significant structural correlations for higher concentration blends. b) Sample with no correlations, which is amenable to the pseudo-thermodynamic approach. (Intensity and q ranges are different for the two graphs.)

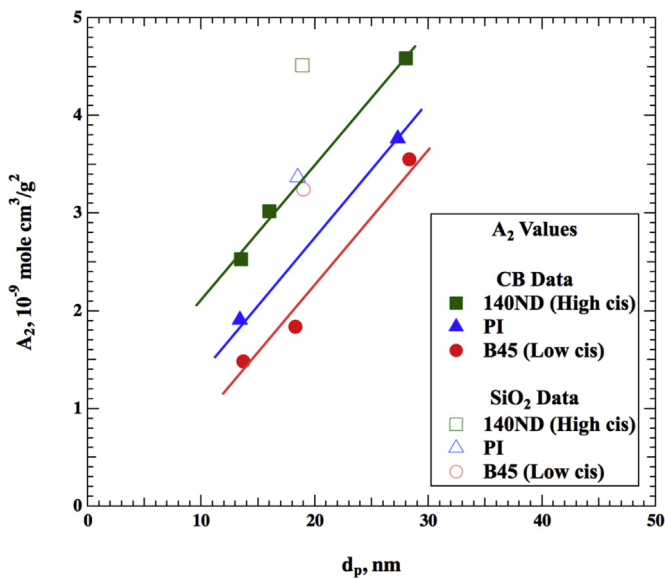


Fig. 6. Pseudo-second order virial coefficient, A_2 , versus primary particle size (Sauter mean diameter or equivalent spherical diameter). Lines are drawn to guide the eye. Larger, positive A_2 indicates better dispersion. (A_2 values are plotted to three significant figures, which is greater than in Table 4.)

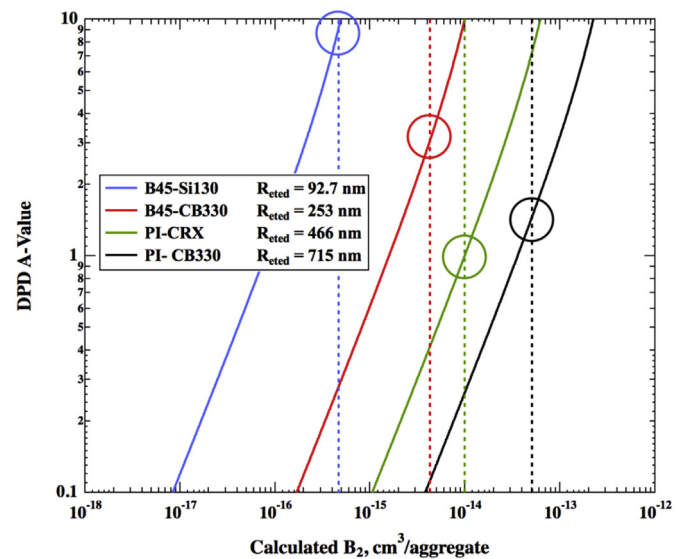


Fig. 7. Calculation from equations (3) and (5) for the mass based second virial coefficient, B_2 , based on the average end-to-end distance from Table 4. Vertical dashed lines show the experimentally measured values for B_2 and circles show the intersection that determines the DPD A -value, the magnitude of the potential function given in equation (5) for a given aggregate size as reflected by the end to end distance, R_{eted} .

scattering correspond to the grey circles in the micrographs. The end-to-end distance for an aggregate as estimated by $d_p p^{1/d_{min}}$, values from Table 3 is $R_{eted} = 254$ nm. An aggregate is expected to be four scale markers. This is reasonably close to what is seen in the first micrograph, two bottom right aggregates, prior to agglomeration. The number of branches per aggregate in Table 3 is $n_{Br} = 0.7$ for N330, and about 1 branch per aggregate, in B45. This also agrees with the two aggregates at the bottom right of Fig. 8a. It should be noted that the TEM samples shown in Fig. 8 are on the order of 80 nm thick so that features at sizes larger than this may be compromised by the sample preparation method described in the Experimental Section.

The percolation concentration follows a fractal scaling law so that $\phi^* \sim M/V = R_{g2}^d/(R_{g2}^3) \sim R_{g2}^{d-3}$. Fig. 9 shows a plot of the

percolation concentration versus R_{g2}^{d-3} for CB and silica samples. In many a monotonic trend is observed. The linear intercept for the CB samples does not pass through (0, 0). A zero intercept is expected since an infinite aggregate should percolate at zero concentration. Silica comes closer to this expectation.

For filled elastomers with filler loading above the overlap concentration (local percolation threshold) the filler particles form a network with a mesh size that decreases with increasing concentration, as shown in Fig. 1. For size scales larger than the mesh size (reflecting large relaxation times) the elastomer properties should be dominated by the filler network, while for size scales smaller than the mesh size (and short relaxation times) the properties are

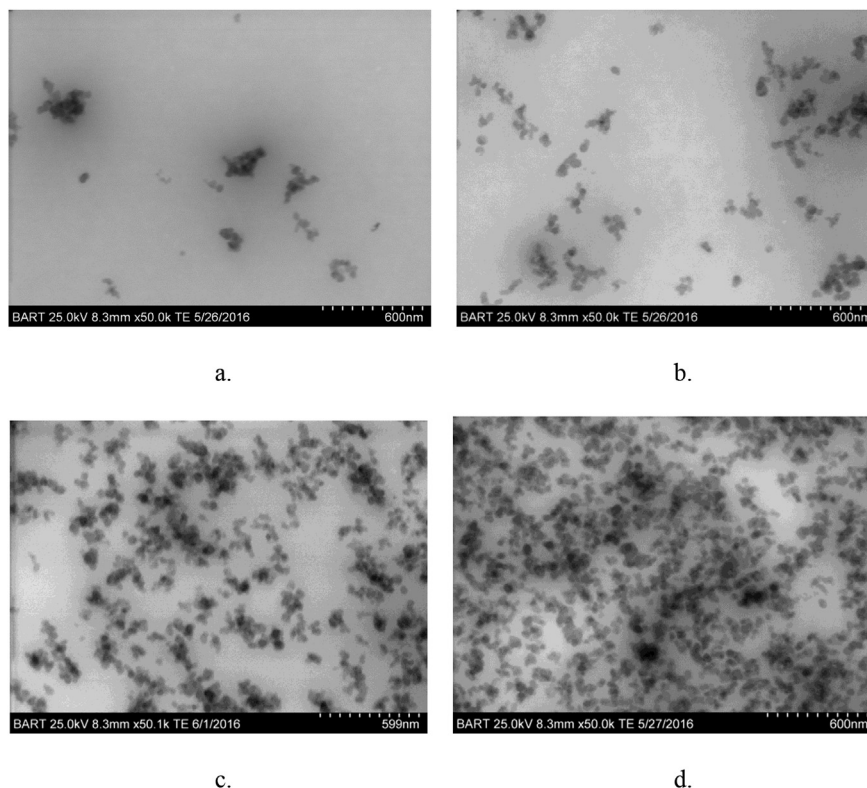


Fig. 8. Scanning transmission electron micrographs of carbon filled elastomers. N330 blended in B45. The weight percent for these samples are 1, 5, 15, and 30, a to d in the figure. The distance between scale markers in the lower right of each of the figures is about 60 nm with the full range being about 600 nm.

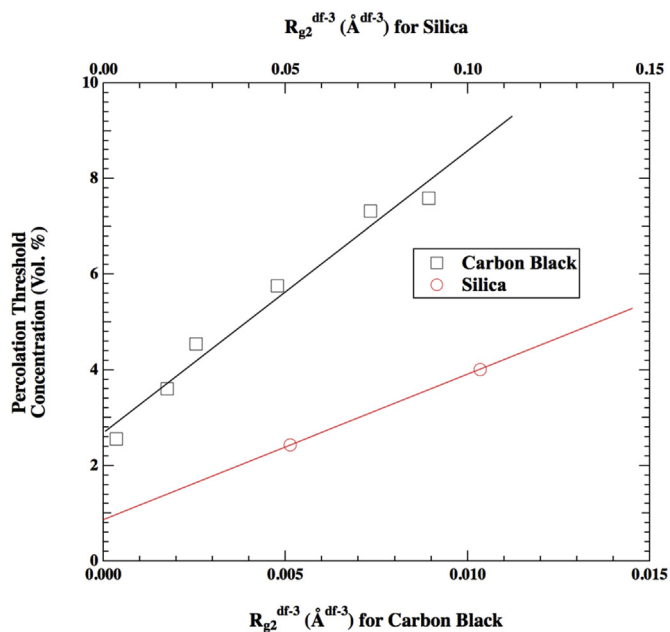


Fig. 9. Percolation threshold concentration of CB and silica as a function of R_{g2}^{df-3} .

dominated by the elastomer. For this reason it is important to quantify the filler network mesh size. The mesh size of the filler network above the percolation threshold concentration is given by $2\pi/q^*$, where q^* is the q value when $1/(\nu\phi)$ equals $I_0(q)/\phi_0$ from the one weight percent scattering curve under dilute conditions for levels 1 and 2. Table 5 shows the mesh sizes calculated in this way

for all of the samples for 15 and 30 wt % filler concentrations. For the same filler, larger mesh size is always observed in samples with a higher percolation threshold. The mesh size decreases with concentration as expected.

The mesh size shown in Table 5 agrees well with the micrographs in Fig. 8. For 15 wt percent the mesh size is about 500 nm, close to the entire range of the scale bar, so it corresponds well to the gaps between aggregate clusters. Similarly, for 30 wt percent the mesh size is about 300 nm, one half of the entire range of the scale bar, which is close to the gaps in the image between dense clusters of aggregates.

5. Conclusion

Immiscible mixtures of nano to colloidal particles in polymers bear some resemblance to colloidal solutions. While colloidal solutions have a random dispersion of particles driven by dynamic thermal equilibrium and are influenced by enthalpic interactions between particles, polymer compounds display a random dispersion of particles driven by the mixing process and influenced by surface interactions between particles. The effectiveness of mixing will depend on particle size, accumulated strain, viscosity of the matrix polymer and the hydrodynamic properties of the nanoparticles being dispersed. It seems possible to apply a pseudo-thermodynamic approach to these systems to quantify the dispersion of a given nanoparticle and polymer binary pair after a certain processing history. This approach can be used to rank different polymer/nanoparticle pairs as to relative dispersion. Reinforced elastomer composites were examined using this new application of the second virial coefficient to describe compatibility of carbon black and silica with three different elastomers. It was found that this approach distinguishes dispersion for different elastomer/filler

compounds. Ultra small-angle X-ray scattering was used to measure the scattering pattern at several concentrations of filler. Changes in scattering with concentration were described with a single second virial coefficient for each elastomer compound using a scattering function related to the random phase approximation. The approach seems applicable to a wide range of nanocomposite materials.

The pseudo-second virial coefficient, A_2 , was well behaved in the PB/PI and CB/SiO₂ compounds that were studied. A close to linear dependence of A_2 with primary particle size for carbon black composites agrees well with the observation that it is more difficult to mix smaller particles. High cis 1,4 polybutadiene displayed better dispersion for carbon and silica compared to low cis 1,4 polybutadiene consistent with literature reports. Silica was better dispersed for the same primary particle size compared to carbon black. Additionally, expected predictions for comparative compatibility between two PB and a PI sample were observed. Further, the interfacial contribution to this compatibility could be ascertained by the sign and value of the $d_p = 0$ intercept of A_2 .

Values for the repulsive interaction potential amplitude, “A” were estimated for the samples from the A_2 values and calculations of R_{eted} . These values could be used in coarse grain computer simulations of filler segregation in these elastomers. The percolation threshold concentration and the mesh size for concentrations above this threshold were determined. Both of these features are well behaved in the samples studied. The results qualitatively agreed with expectations and with micrographs.

This study presents a novel pseudo-thermodynamic description of polymer nanocomposites that shows promise in predicting dispersibility and compatibility in complex compounds based on processing history and tabulated values for A_2 . The approach is quite general and could be applied to pigment dispersions and many other polymer/nanoparticle composites.

Acknowledgements

Data were collected at the X-ray Science Division beamline 9ID at the Advanced Photon Source, Argonne National Laboratory. This research used resources of the Advanced Photon Source, a U.S. Department of Energy (DOE) Office of Science User Facility operated for the DOE Office of Science by Argonne National Laboratory under Contract No. DE-AC02-06CH11357. This work was supported by the National Science Foundation through grants CMMI-1635865 and CMMI-1636036.

Appendix A. Supplementary data

Supplementary data related to this article can be found at <https://doi.org/10.1016/j.polymer.2017.09.040>.

References

- [1] T.A. Witten, M. Rubinstein, R.H. Colby, Reinforcement of rubber by fractal aggregates, *Phys. Rev. Lett.* 3 (1993) 367–383.
- [2] J.L. Leblanc, *Filled Polymers: Science and Industrial Applications*, CRC Press, Boca Raton, FL, 2010.
- [3] S. Wolff, M.J. Wang, Carbon black reinforcement of elastomers, in: J.B. Donnet, R.C. Bansal, M.J. Wang (Eds.), *Carbon Black*, Marcel Dekker, New York, 1993.
- [4] D. Goritz, H. Raab, J. Fröhlich, P.G. Maier, Surface structure of carbon black and reinforcement, *Rub. Chem. Tech.* 72 (1999) 929–945.
- [5] B.P. Kavgate, C. Das, D. Basu, A. Das, G. Heinrich, Rubber composites based on silane-treated stober silica and nitrile rubber: interaction of treated silica with rubber matrix, *J. Elast. Plastics* 47 (2015) 248–261.
- [6] J. Abraham, H.J. Maria, S.C. George, N. Kalarikkal, S. Thomas, Transport characteristics of organic solvents through carbon nanotube filled styrene

- butadiene rubber nanocomposites: the influence of rubber-filler interaction, the degree of reinforcement and morphology, *Phys. Chem. Chem. Phys.* 17 (2015) 11217–11228.
- [7] C.R. Herd, G.C. McDonald, W.M. Hess, Morphology of carbon-black aggregates—fractal versus euclidean geometry, *Rub. Chem. Tech.* 65 (1992) 107–129.
- [8] C.R. Herd, G.C. McDonald, R.E. Smith, W.M. Hess, The use of skeletonization for the shape classification of carbon-black aggregates, *Rub. Chem. Tech.* 66 (1993) 491–509.
- [9] T. Koga, T. Hashimoto, M. Takenaka, K. Aizawa, N. Amino, M. Hakamura, D. Yamaguchi, S. Koizumi, New insight into hierarchical structures of carbon black dispersed in polymer matrices: a combined small-angle scattering study, *Macromolecules* 41 (2008) 453–464.
- [10] K.W. Stöckelhuber, A. Das, R. Jurk, G. Heinrich, Contribution of physico-chemical properties of interfaces on dispersibility adhesion and flocculation of filler particle in rubber, *Polymer* 51 (2010) 1954–1963.
- [11] K.W. Stöckelhuber, A.S. Svistkov, A.G. Pelevin, G. Heinrich, Impact of filler surface modification on large scale mechanics of styrene butadiene/silica rubber composites, *Macromolecules* 44 (2011) 4366–4381.
- [12] B. Natarajan, Y. Li, H. Deng, L.C. Brinson, L.S. Schadler, Effect of interfacial energetics on dispersion and glass transition temperature in polymer nanocomposites, *Macromolecules* 46 (2013) 2833–2841.
- [13] I. Hassinger, X. Li, H. Zhao, H. Xu, Y. Huang, A. Prasad, L. Schadler, W. Chen, L.C. Brinson, Toward the development of a quantitative tool for predicting dispersion of nanocomposites under non-equilibrium processing conditions, *J. Mat. Sci.* 51 (2016) 4238–4249.
- [14] K.W. Stöckelhuber, S. Weißner, A. Das, G. Heinrich, Filler flocculation in polymers – a simplified model derived from thermodynamics and game theory, *Soft Matter* 13 (2017) 3701–3709.
- [15] G. Beaucage, R. Composto, R.S. Stein, Ellipsometric study of the glass transition and thermal expansion coefficient of thin polymer films, *J. Polym. Sci. Pt. B, Polym. Phys.* 31 (1993) 319–326.
- [16] N. Patel, S.A. Egorov, Interactions between colloidal particles in polymer solutions: a density functional theory study, *J. Chem. Phys.* 121 (2004) 4987–4997.
- [17] A. Bymaster, S. Jain, W.G. Chapman, Microstructure and depletion forces in polymer-colloid mixtures from an interfacial statistical associating fluid theory, *J. Chem. Phys.* 128 (2008) 164910.
- [18] E.N. Mintsas, P. Germain, S. Amokrane, Bond lifetime and diffusion coefficient in colloids with short-range interactions, *Euro. Phys. J. E. Soft Mat.* 38 (2015) 21–31.
- [19] F. Bonneté, S. Finet, A. Tardieu, Second virial coefficient: variations with lysozyme crystallization conditions, *J. Cryst. Growth* 196 (1999) 403–414.
- [20] P.B. Warren, A. Vlasov, L. Anton, A.J. Masters, Screening properties of Gaussian electrolyte models, with application to dissipative particle dynamics, *J. Chem. Phys.* 138 (2013) 204907.
- [21] M. Takenaka, Analysis of structures of rubber-filler systems with combined scattering methods, *Polym. J.* 45 (2013) 10–19.
- [22] G. Beaucage, H.K. Kammler, S.E. Pratsinis, Particle size distributions from small-angle scattering using global scattering functions, *J. Appl. Cryst.* 37 (2004) 523–535.
- [23] G. Beaucage, Determination of branch fraction and minimum dimension of mass-fractal aggregates, *Phys. Rev. E* 70 (2004) 031401.
- [24] H.K. Kammler, G. Beaucage, R. Mueller, S.E. Pratsinis, Structure of flame-made silica nanoparticles by ultra-small-angle x-ray scattering, *Langmuir* 20 (2004) 1915–1921.
- [25] R. Ramachandran, G. Beaucage, D. McFaddin, J. Merrick-Mack, V. Galiatatos, F.M. Mirabella, Branch length distribution in TREF fractionated polyethylene, *Polym* 52 (2011) 2661–2666.
- [26] R. Ramachandran, G. Beaucage, A.S. Kulkarni, D. McFaddin, J. Merrick-Mack, V. Galiatatos, Branch content of metallocene polyethylene, *Macromolecules* 42 (2009) 4746–4750.
- [27] A.S. Kulkarni, G. Beaucage, Quantification of branching in disordered materials, *J. Polym. Sci. B-Polym. Phys.* 44 (2006) 1395–1405.
- [28] A.S. Kulkarni, G. Beaucage, Investigating the molecular architecture of hyperbranched polymers, *Macromol. Rapid Comm.* 28 (2007) 1312–1316.
- [29] K. Vogt, G. Beaucage, H. Jiang, M. Weaver, Thermodynamic stability of worm-like micelle solutions, *Soft Matter* 13 (2017) 6068–6078.
- [30] P.M. Doty, B.H. Zimm, H. Mark, Some light scattering experiments with high polymer solutions, *J. Chem. Phys.* 12 (1944) 144, 144.
- [31] P.M. Doty, B.H. Zimm, H. Mark, An investigation of the determination of molecular weights of high polymers by light scattering, *J. Chem. Phys.* 13 (1945) 159–166.
- [32] J. Pedersen, C. Sommer, Temperature dependence of the virial coefficients and the chi parameter in semi-dilute solutions of PEG, *Prog. Coll. Polym. Sci.* 130 (2005) 70–78.
- [33] L. Song, Z. Wang, X. Tang, L. Chen, P. Chen, Q. Yuan, L. Li, Visualizing the toughening mechanism of nanofiller with 3D X-ray nano-CT: stress-induced phase separation of silica nanofiller and silicone polymer double networks, in press, *Macromolecules* (2017), <http://dx.doi.org/10.1021/acs.macromol.7b00539>.
- [34] www.firesyn.com/pdf/140ND-Diene-Rubber-Grade-tds.pdf.
- [35] https://techcenter.lanxess.com/pbr/emea/en/products/datasheet/Buna_CB_

- 45.pdf?docId=14093518&gid=14091459&pid=6.
- [36] T. Koga, M. Takenaka, K. Aizawa, M. Nakamura, T. Hashimoto, Structure factors of dispersible units of carbon black filler in rubbers, *Langmuir* 21 (2005) 11409–11413.
- [37] J. Ilavsky, P.R. Jemian, A.J. Allen, F. Zhang, L.E. Levine, G.G. Long, Ultra-small-angle x-ray scattering at the advanced photon source, *J. Appl. Cryst.* 42 (2009) 469–479.
- [38] N.M.T. Pires, A.A. Ferreira, C.H. de Lira, P.L.A. Coutinho, L.F. Nicolini, B.G. Soares, F.M.B. Coutinho, Performance evaluation of high-cis 1,4-polybutadienes, *J. Appl. Polym. Sci.* 99 (2006) 88–99.
- [39] C.P. O'Farrell, M. Gerspacher, L. Nikiel, Carbon black dispersion by electrical measurements, *Kaut. Gummi Kunstst.* 53 (2000) 701–710.